Science and Innovation of Advanced Materials

The Materials Research Society of Thailand

Research Article

Characterization and Visible Light-driven Photocatalytic Activity of $SnS_2/BiVO_4$ Nanocomposites Prepared by Sonochemical-based Process

Thanaphon Kansaard*, Maneerat Songpanit, Wisanu Pecharapa

College of Materials Innovation and Technology, King Mongkut's Institute of Technology Ladkrabang, Bangkok 10520, Thailand

* Corresponding author e-mail: tkansaard@gmail.com

Received: *December 1st, 2023* | ***Revised:*** *January 30th, 2024* | ***Accepted:*** *January 30th, 2024*

Abstract: Bismuth vanadate ($BiVO_4$) is a good candidate photocatalyst material with good activity under visible light exposure. The photodecomposition performance of $BiVO_4$ could be enhanced by combining it with compatible tin sulfide (SnS_2). In this work, the synthesis of $SnS_2/BiVO_4$ nanocomposite was carried out by sonochemical process at room temperature with varying concentration ratios of SnS_2:$BiVO_4$ (0.05:1, 0.10:1, 0.15:1, 0.50:1 and 1:1). The crystallinity and morphological features of as-synthesized powders demonstrate the majority of $BiVO_4$ monoclinic phase accompanying minority of SnS_2 rhombohedral phase. FE-SEM micrograph shows the irregular shape with various particle sizes. The optical band gap of the composite inquired by Kubellka-Munk calculation is about 2.6 eV. The photocatalytic performance of as-synthesized nanocomposite was evaluated by means of decomposition of organic dye under visible light irradiation. The 0.05:1 ratio of the $SnS_2/BiVO_4$ sample exhibits superior photocatalytic activity with 60% decomposition of Rhodamine-B organic dye within 120 minutes.

Keywords: Bismuth vanadate, Tin sulfide, Nanocomposite, Photocatalyst material

1. Introduction

Recently, environmental pollution, including heavy metal toxicity, wastewater, and organic compounds from industry has become a greatly critical issue to be effectively solved. There are number of practical treatment processes for curing highly toxic waste to be less or non-toxic, for example, porous carbon as an absorber or photocatalytic material for larger organic molecules decomposition. Metal oxide semiconductor photocatalyst materials, including titanium dioxide (TiO_2), zinc oxide (ZnO), and bismuth vanadate ($BiVO_4$) based materials, have exhibited good photocatalytic performance under UV and visible light irradiation [1,2]. Among them, $BiVO_4$ becomes a promising candidate due to considerably high photocatalytic activity under visible light exposure. Furthermore, the development of functional materials in the form of heterojunction between two or more different materials is an interesting issue due to the significant enhancement of free carrier transport and photogenerated electron-hole separation leading to amelioration in photocatalytic activity [3,4]. SnS_2 material is one of the potential candidate semiconductors for incorporation with $BiVO_4$ because of its narrow band gap energy of 2.4 eV and good ability to generate free radicals

for organic compound decomposition [5,6]. Generally, $BiVO_4$ and other metal oxide semiconductor materials can be synthesized via various methods such as the co-precipitation method, solid state reaction, and hydrothermal and sonochemical processes. Among these processes, sonochemical processes have significant advantages, including noncomplex, rapid reaction, and needless thermal treatment [7-9].

This article represents sonochemical synthesis of $SnS_2/BiVO_4$ nanocomposite with various SnS_2 loading compositions in $BiVO_4$ that can be utilized as visible-light-driven photocatalytic material. Structural, morphological, optical, and photocatalytic properties of the prepared composites are extensively investigated.

2. Methodology

2.1 Materials

Bismuth nitrate pentahydrate ($Bi(NO_3)_3{\cdot}5H_2O$, 98% purity) from KemAus chemical company while ammonium metavanadate (NH_4VO_3, 99.5% purity) analytical grade from Ajax Finechem were used for bismuth (Bi) and vanadium (V) starting material, respectively. For tin (Sn) and sulfur (S), tin(IV)chloride pentahydrate ($SnCl_4{\cdot}5H_2O$, ≥ 98% purity) and thioacetamide chemical reagents purchased from Sigma Aldrich were used, respectively.

2.2 Methods

Preparation of $BiVO_4$

$BiVO_4$ nanoparticles were synthesized through a single-step sonochemical process without subsequent thermal treatment. Initially, $Bi(NO_3)_3{\cdot}5H_2O$ and NH_4VO_3, with a stoichiometric mole ratio of 1:1, were separately dissolved in deionized (DI) water and continuously stirred for 10 minutes at room temperature. Subsequently, the solutions of Bi and V precursors were combined, and the pH was adjusted to 7 with ammonia solution until a yellow solution was achieved. The resulting mixed solution was then transferred to a sonochemical flask reactor, where the process was conducted under 750 W ultrasonic irradiation operating at 20 kHz for 30 minutes at room temperature, resulting in the formation of a yellowish suspension. The precipitated product was thoroughly washed with deionized water multiple times until reaching a neutral pH to eliminate any undesirable components. Subsequently, the precipitate was dried overnight, resulting in the formation of a dark yellow powder.

Preparation of $SnS_2/BiVO_4$ nanocomposite

The $SnS_2/BiVO_4$ nanocomposites were synthesized using a procedure analogous to that employed for $BiVO_4$ nanoparticles as following previous work [10]. Specifically, $SnCl_4{\cdot}5H_2O$ was dissolved in a solution of deionized (DI) water and hydrochloric acid (HCl). In contrast, the sulfur precursor, thioacetamide, was dissolved in DI water at 50 °C under continuous stirring until a clear solution was obtained. Subsequently, the two starting solutions were combined, and the as-prepared $BiVO_4$ powder was introduced into the mixture with designated $SnS_2/BiVO_4$ ratios of 0.05:1, 0.10:1, 0.15:1, 0.50:1, and 1:1. The resulting suspension was stirred for an additional 10 minutes. Ultrasonic irradiation (750 W, 20 kHz) was then applied to the sonochemical flask chamber containing the mixed solution for 30 minutes to achieve a yellowish/brownish suspension. The resulting composites, featuring varying SnS_2 loading contents, were washed with DI water and dried at 100 °C to obtain the nanocomposite specimens. The samples were labeled based on the SnS_2:$BiVO_4$ ratio, signifying the composition of SnS_2 loading in the composite.

Materials characterization

The crystalline structure of all specimens was examined using the X-ray diffraction (XRD) technique with a Cu$K\alpha$ X-ray source and a Rigaku SmartLab model. Chemical bonding in the as-synthesized samples was analyzed using a Raman spectrometer (Thermo Scientific, DXR SmartRaman model). Optical properties were assessed through diffuse reflectance spectroscopy (DRS) using a HITACHI spectrophotometer UH1450 model, with the optical band gap calculated using the Kubelka-Munk equation. Surface characteristics were observed using field emission scanning

electron microscopy (FESEM) JSM-7001F model, and the morphology and chemical composition were further analyzed using an energy dispersive X-ray spectrometer (EDX) Oxford, INCA PentaFETx3 model. Additionally, the specific surface area was determined through the Brunauer-Emmett-Teller method (BET) using the Quantachrome Autosorb iQ-C-XR-XR-XR model.

Photocatalytic testing

The photocatalytic efficiency of the composite was assessed by photodegrading Rhodamine B (RhB), an organic dye considered representative of organic pollution, under visible light exposure. A quantity of 0.1 g of the photocatalyst was introduced into a 50 ml solution containing 10 μM of RhB. The mixture was stirred in the absence of light (stored in a dark reactor) for 30 minutes to establish equilibrium in terms of absorption/desorption on the photocatalyst surface. Subsequently, visible light generated by a cool daylight LED strip was directed onto the reactor while constant stirring was maintained. Every 10 minutes, 10 mL of the solution was withdrawn and centrifuged to separate the precipitate from the solution, facilitating the analysis of the remaining RhB in the solution. The photodegradation rate of RhB by the prepared photocatalyst was determined using the equation: Degradation rate = A/A_i where A represents the absorption intensity of RhB at any given time, and A_i denotes the absorption intensity of RhB at the initiation of the reaction.

3. Results and discussion

Crystalline structure

The diffractograms of all specimens are shown in Figure 1. The X-ray diffraction (XRD) results reveal the predominant diffraction pattern of the $BiVO_4$ monoclinic phase, evident at 2θ values of 18.9°, 28.9°, 29.4°, 34.9°, 42.6°, 47.0°, 50.2°, 53.3°, 58.4°, and 59.5° (JCPDS No. 01-083-1699). Conversely, the as-prepared SnS_2 exhibits diffraction broad peaks at 2θ = 25.9° and 33.5°, corresponding to the SnS orthorhombic phase (JCPDS No. 00-053-0526) and the SnS_2 hexagonal phase (JCPDS No. 01-089-2358), respectively. During the sonochemical process, the possible chemical reactions for forming $BiVO_4$ and SnS_2 could be explained following Equations 1-3 and 4-7, respectively [11,12]. For the composite sample, the diffraction pattern of the $BiVO_4$ monoclinic phase can be observed as the main phase. As the SnS_2 loading content in the composite was increased up to 15%, the XRD still remained in the pure monoclinic phase. Thereafter the appearance of secondary phase of $BiVO_4$ tetragonal phase located at 2θ = 24.4° and 32.6° could be observed. This feature suggests that the higher loading content of SnS_2 could induce the phase transformation of $BiVO_4$. Based on the XRD results, it is evident that the nanocomposite, formed through a sonochemical process, comprises coexisting phases of $BiVO_4$ and SnS_2.

$$Bi(NO_3)_3 + H_2O \rightarrow BiONO_3 + 2HNO_3 \quad (1)$$

$$NH_4VO_3 + H_2O \rightarrow HVO_4 + NH_4OH \quad (2)$$

$$BiONO_3 + HVO_4 \rightarrow BiVO_4 + HNO_3 \quad (3)$$

$$SnCl_4 + 5H_2O \rightarrow SnO_2 + 4HCl + 3H_2O \quad (4)$$

$$SnO_2 + 4HCl \rightarrow Sn^{4+} + 4Cl^- + 2H_2O \quad (5)$$

$$CH_3(C=S)NH_2 + H_2O \rightarrow CH_3(C=O)NH_2 + H_2S \quad (6)$$

$$2H_2S + Sn^{4+} \rightarrow SnS_2 + 4H^+ \quad (7)$$

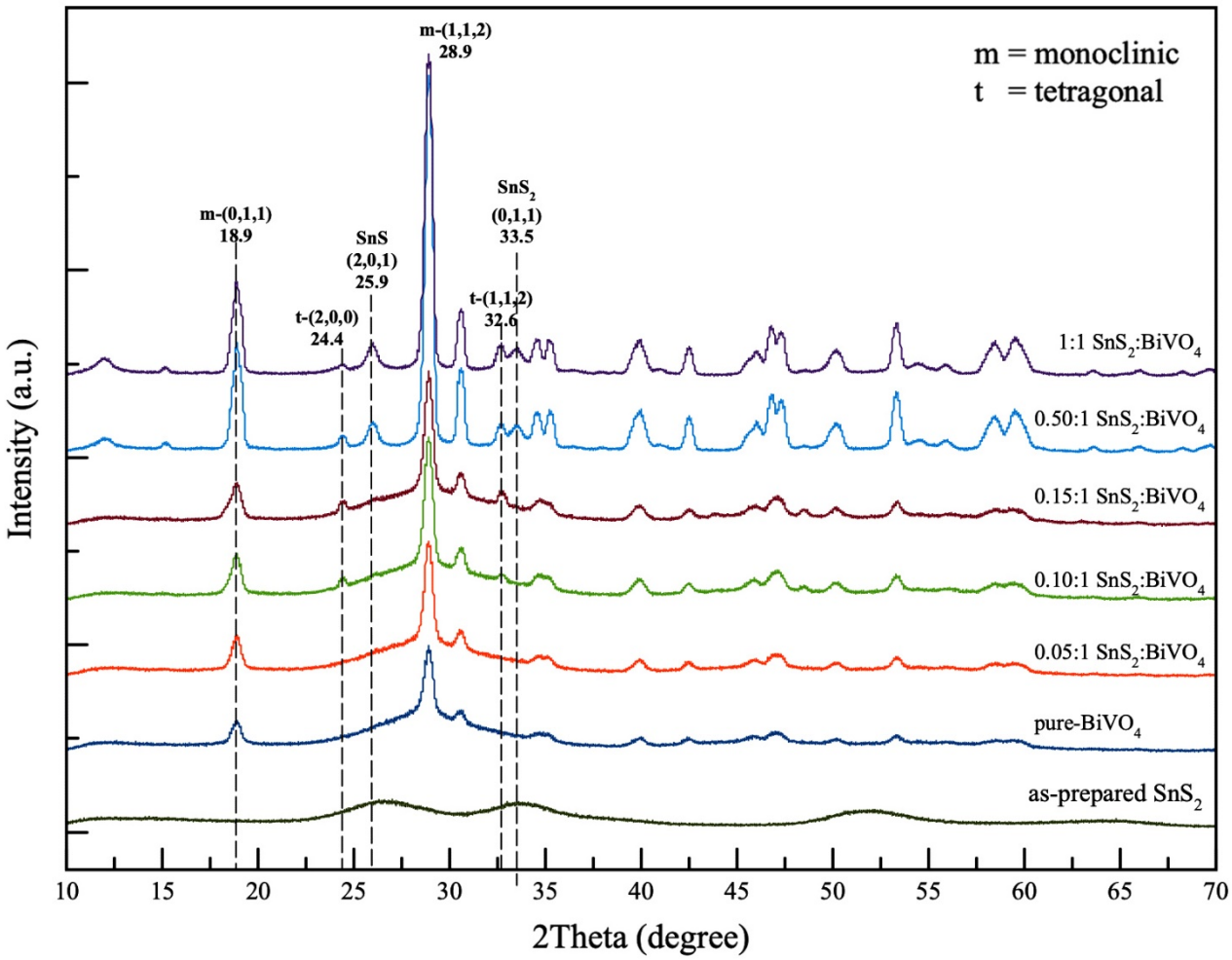

Figure 1 X-ray spectra of nanocomposite with different composition ratios of SnS_2 and $BiVO_4$.

Chemical bonding

The chemical bondings of the $SnS_2/BiVO_4$ composite were determined by the Raman scattering technique (Figure 2). The as-prepared SnS_2 powder exhibits the vibration peaks at Raman-shift of 311 cm^{-1} relating to the A_{1g} vibration mode of SnS_2 [13,14] and the broad peak at 553 cm^{-1}. The bare $BiVO_4$ and all composite samples with different compositions express the same feature of Raman-shift located at 812 cm^{-1} correlating to the V-O symmetric stretching mode and peak positions at 368 cm^{-1} and 327 cm^{-1}, indicating a coexistence of symmetric and asymmetric bending modes of VO_4^{3-} tetrahedral group. The deformation and overlapping of these two peaks of the VO_4^{3-} bending mode with decreasing intensity could be due to the different formation and shapes of particles that can be observed in the FESEM photograph (Figure 4). Other couple peaks positioned at 197 cm^{-1} and 115 cm^{-1} are ascribed to typical external modes of $BiVO_4$ monoclinic crystal [15,16].

Optical property

The diffuse reflectance spectrum of the bare $BiVO_4$ sample in Figure 3(a) shows the prominent absorption edge at 450 nm. In comparison, the as-prepared SnS_2 powder exhibits the lowering reflection spectra covering the broad visible wavelength region of 450-600 nm, reflecting higher absorptivity in this wavelength region. For $SnS_2/BiVO_4$ nanocomposite specimen with SnS_2:$BiVO_4$ ratios of 0.05:1 – 0.15:1, a similar absorption edge to bare $BiVO_4$

sample is noticed due to the dominant absorption of $BiVO_4$ matrix material. As the component of the SnS_2:$BiVO_4$ ratio increases to reach 0.5:1 and 1:1, the absorption edge of the sample exhibits a slight redshift to 475 nm, as observed in Figure 3(a). The optical band gaps of all samples were calculated via the Kubelka-Munk equation as following

$$F(R) = \frac{(1-R)^2}{2R}$$

where R referring the reflectance value, and the corresponding results are depicted in Figure 3(b). The calculated optical band gap of as-prepared $BiVO_4$ and SnS_2 powder are approximately 2.55 eV and 2.34 eV, respectively. The small loading of SnS_2 (0.05-0.15) in composite samples exhibited a slight shift in the optical band gap, approximately 2.55 eV. On the other hand, higher SnS_2 content (0.5-1.0) revealed a redshift towards a smaller band gap, approximately 2.5 eV. However, band gaps of the composites are determined to be approximately 2.5 eV, positioned between the individual band gaps of the two materials. This observation signifies a modification in the band gap of the $BiVO_4$ matrix due to the incorporation of SnS_2. Furthermore, the composite structure with SnS_2 indicates an enhancement in visible light absorption for $BiVO_4$, suggesting its suitability as a visible light-driven photocatalyst bridging the properties of these two materials [17].

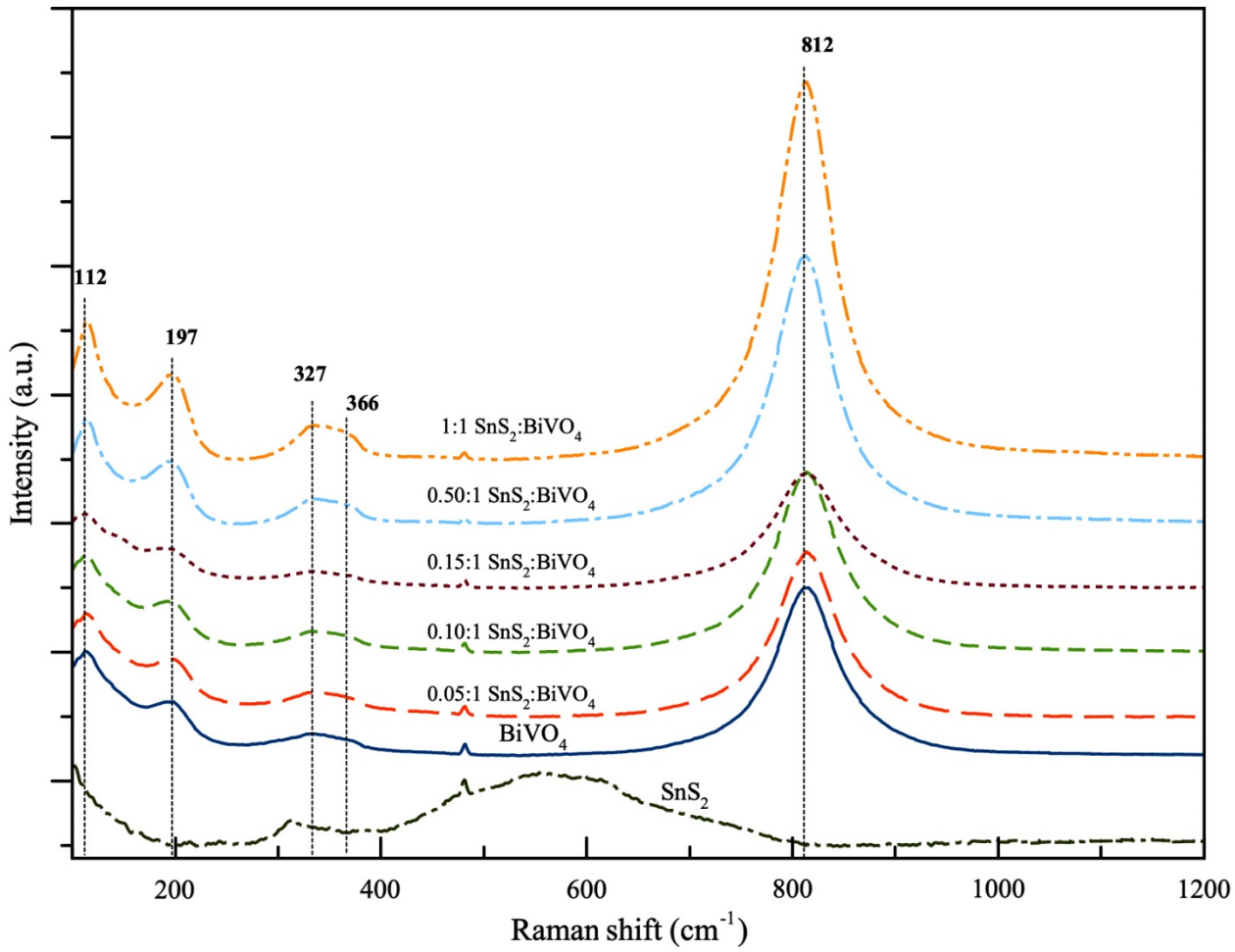

Figure 2 Raman spectra of as-prepared SnS_2, bare $BiVO_4$, and x-SnS_2/$BiVO_4$ composites.

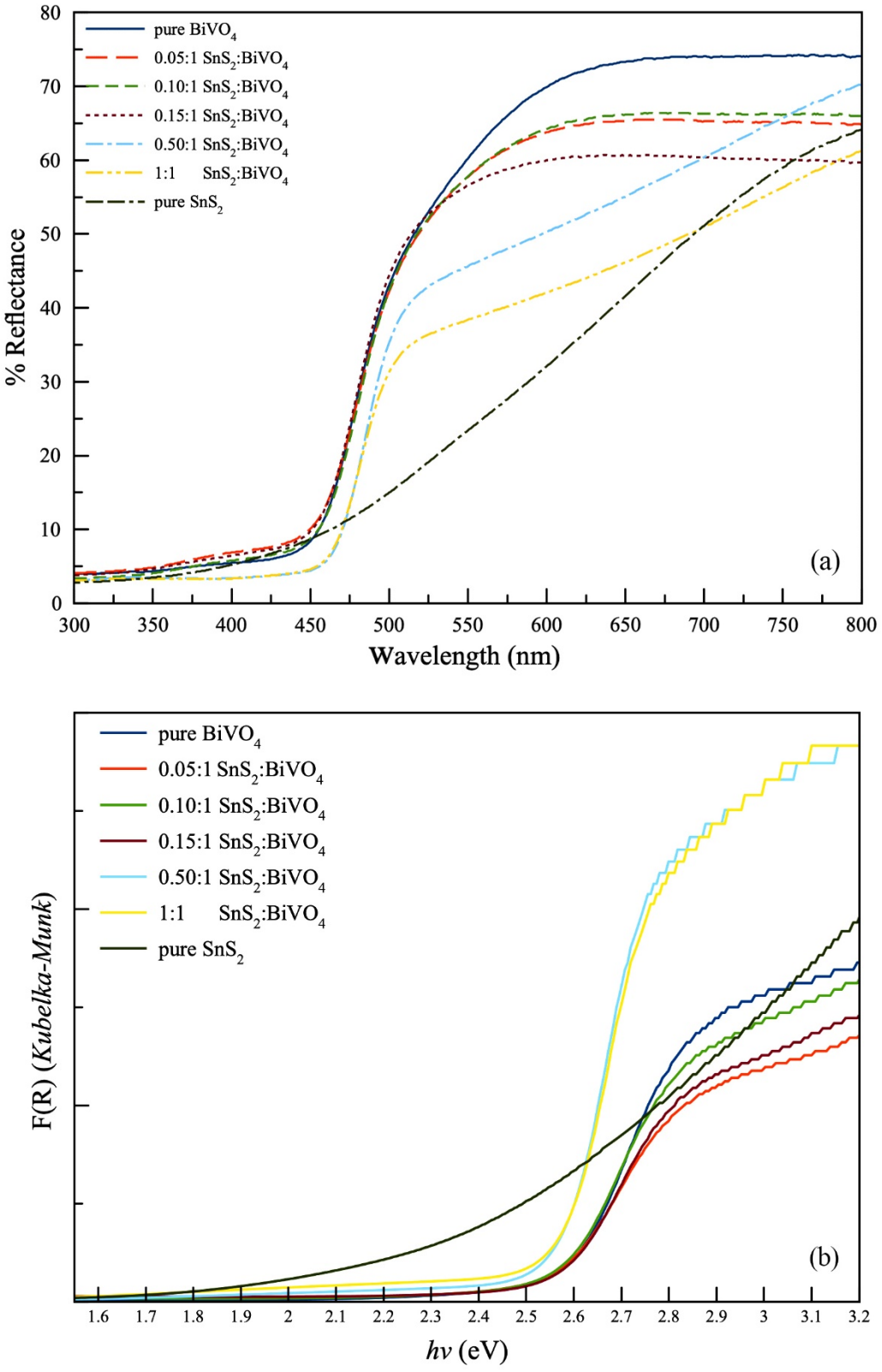

Figure 3 (a) Diffuse reflectance spectra of as-prepared SnS_2, $BiVO_4$, and $SnS_2/BiVO_4$ composite sample and (b) optical band gap of all specimens calculated by using Kubelka-Munk equation.

Morphology

Figure 4(a-b), (c-d), (e-f), and (g-h) illustrate the lowly and highly magnified FE-SEM images of bare $BiVO_4$, 0.05:1, 0.10:1 SnS_2:$BiVO_4$ samples and as-prepared SnS_2, respectively. The appearance of bare $BiVO_4$ is found in a small particle feature with an irregular shape with a particle size of 70-80 nm, as shown in Figure 4(a-b). For the sample with a 0.05:1 ratio of SnS_2:$BiVO_4$, the particles with various sizes and shapes are formed and agglomerated to become a big cluster of 0.5-1 μm. Further increasing SnS_2 content in the composite to a ratio of 0.10:1, its morphology, as shown in Figure 4(e-f) reveals the greater aggregation of tiny particles surrounding the large flake-like structure. Otherwise, the FE-SEM micrograph of pristine SnS_2 (Figure 4(g-h)) demonstrates the larger crystal with observable fracture. The cluster of particles surrounding the large crystal, as shown in the sample with a ratio of 0.05:1 and 0.10:1, indicates the formation of small $BiVO_4$ particles firmly adhered to the SnS_2 crystal surface, suggesting the possible formation of heterojunction between two materials in the form of composite. The chemical elements present in the composite sample were analyzed using EDX, as illustrated in Figure 4(i). The EDX spectrum of the 0.05:1 SnS_2/$BiVO_4$ sample confirmed the presence of various chemical elements in the composite, including Bi, V, O, Sn, and S components. This analysis confirms the formation of a heterojunction between SnS_2 and $BiVO_4$ in the samples. The junction could enhance the photogenerated electron and hole during illumination and retard the recombination of electron-hole due to the difference of conduction and valence band levels as proposed in the schematic energy band diagram (Figure 5) of hetero-photocatalyst material including SnS_2/$BiVO_4$ nanocomposite [18].

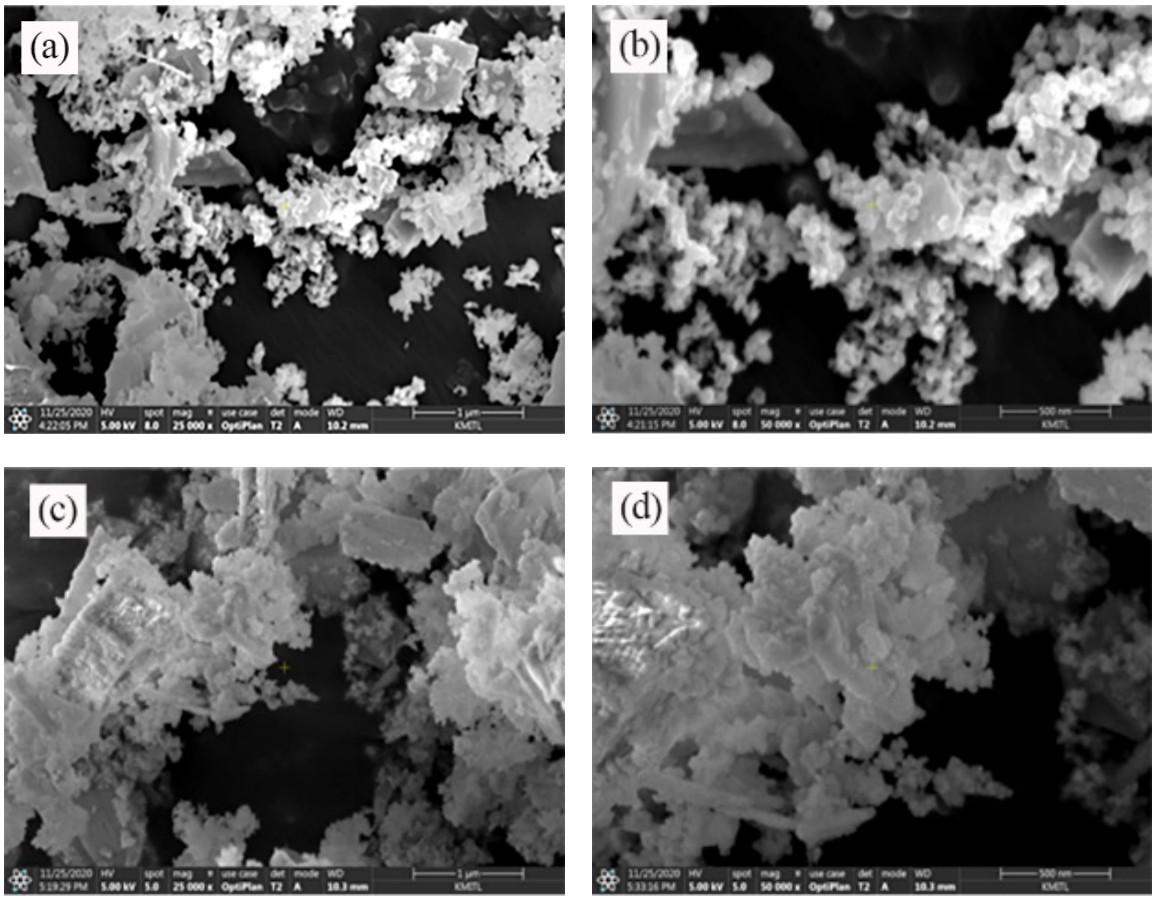

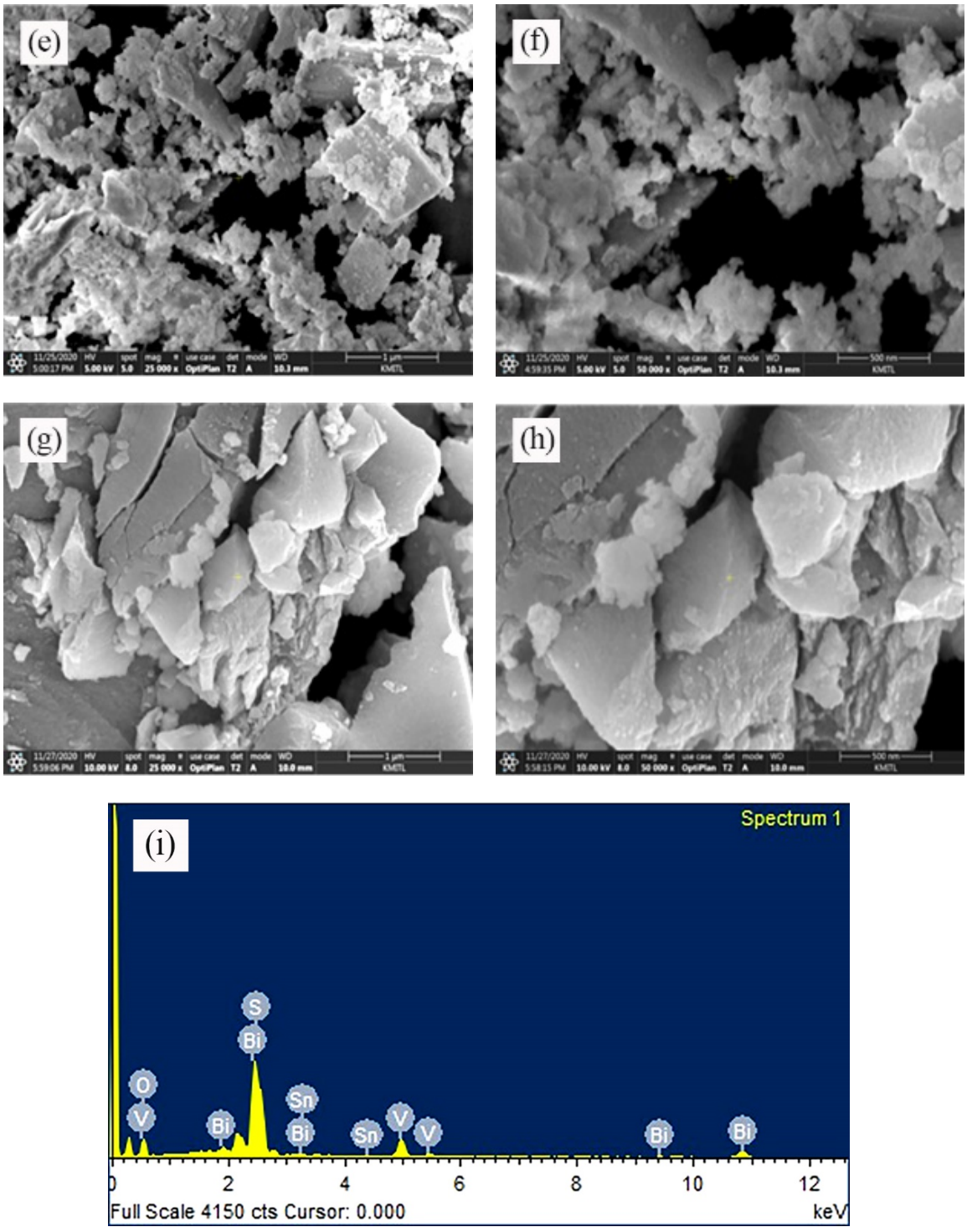

Figure 4 FESEM micrograph of (a,b) bare $BiVO_4$, (c,d) 0.05:1, (e,f) 0.10:1, (g,h) as-prepared SnS_2 samples and (i) EDX spectrum of 0.05:1 composite sample.

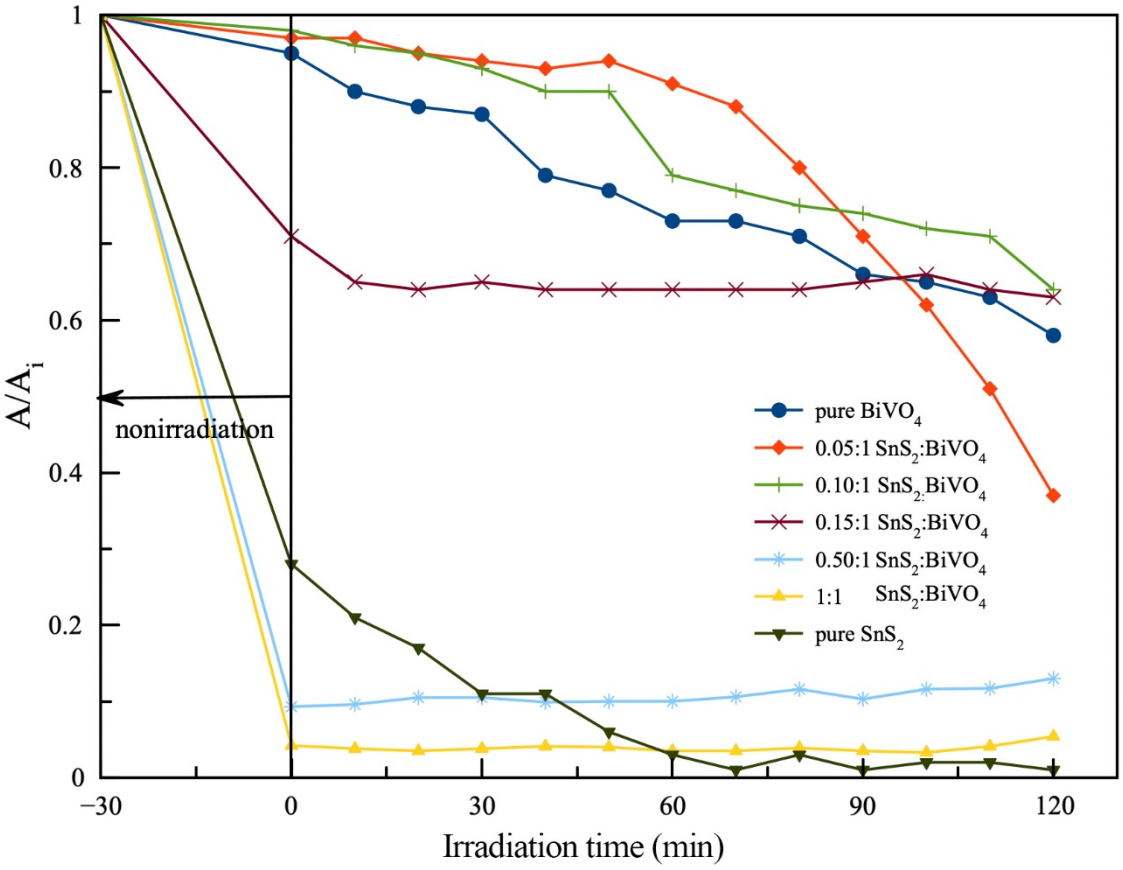

Figure 5 Photocatalytic activity of all nanocomposite photocatalysts under visible light irradiation in terms of A/A_i and irradiation time.

Photocatalytic performance

The photocatalytic activities of the prepared samples were evaluated by the decomposition of Rhodamine B (RhB), an organic dye that acts as organic pollution under visible light exposure. The photocatalytic decomposition graph in terms of A/A_i versus irradiation time is shown in Figure 5. After irradiation with visible light for 120 minutes, pure $BiVO_4$ exhibits a 40% decreasing dye concentration. While pure SnS_2 demonstrated an almost 70% reduction in concentration after stirring in dark conditions, complete dye decomposition was achieved within 120 minutes of irradiation. This remarkable performance in absorption capability on the catalyst surface is evident from the 70% reduction in RhB concentration without any light irradiation, attributed to the highest specific surface area of the bare SnS_2 sample, as illustrated in Table 1. The surface absorption on the SnS_2 sample resulted in a significant reduction in RhB dye concentration, leading to the complete degradation of RhB after 120 minutes of light exposure. The decrease in concentration, correlated with the dose ratio of catalyst and organic compound, is identified as a crucial parameter influencing photocatalytic performance [19].

The decrease in dye concentration under dark conditions is due to the excellent physical adsorption behavior of SnS_2 material, which can be interpreted by the high specific surface area of the as-prepared SnS_2 photocatalyst of approximately 170 m^2/g, as shown in Table 1. Meanwhile, the BET surface area of bare $BiVO_4$ is about 40 m^2/g, resulting in smaller dye adsorption under dark conditions. The photodecomposition of the SnS_2:$BiVO_4$ sample with a ratio of 0.05:1 indicates increasing photocatalytic activity of almost 70% degradation of RhB dye after 120 minutes under visible

light exposure even its low specific surface area of 38 m^2/g. The further increase in SnS_2 content to the ratio of 0.1:1 exhibits inferior catalytic performance of approximately 40% in dye degradation.

Table 1 Specific surface area measurement by N_2 absorption-desorption technique

Samples	Specific surface area (m^2/g)
pure $BiVO_4$	40
0.05:1 SnS_2:$BiVO_4$	38
0.10:1 SnS_2:$BiVO_4$	35
0.15:1 SnS_2:$BiVO_4$	37
0.50:1 SnS_2:$BiVO_4$	44
1:1 SnS_2:$BiVO_4$	75
as prepared SnS_2	170

Moreover, further increasing SnS_2 content beyond this content (0.5:1 – 1:1) results in excellent dye adsorption of SnS_2 instead of decomposition. From the results, incorporating SnS_2 into $BiVO_4$ matrix with certain loading content can significantly enhance photocatalytic performance of the $BiVO_4$ and SnS_2 content plays a significant role in the photocatalytic activity and surface absorption behavior. With small SnS_2 loading, well-defined heterojunctions between SnS_2 and $BiVO_2$ can be formed, as proposed in Figure 6, accompanying the high surface area of the composite. This formation could effectively inhibit the recombination of electron-holes generated during light illumination [20,21]. Under illumination, $BiVO_4$ is responsible for generating holes that can be directly transported to the valence band of SnS_2, where the hydroxyl radical (•OH-) can be produced by reacting with water molecules. Whist, the excited electron on the conduction band of SnS_2 could migrate to the conduction band of $BiVO_4$. At this stage, the electron and hole are well separated so that the electron has enough time to react with O_2 to generate O_2^{2-} radicals for dye decomposition. [22-25]. However, overloading of SnS_2 could lead to the dominance of dye absorption rather than photodegradation.

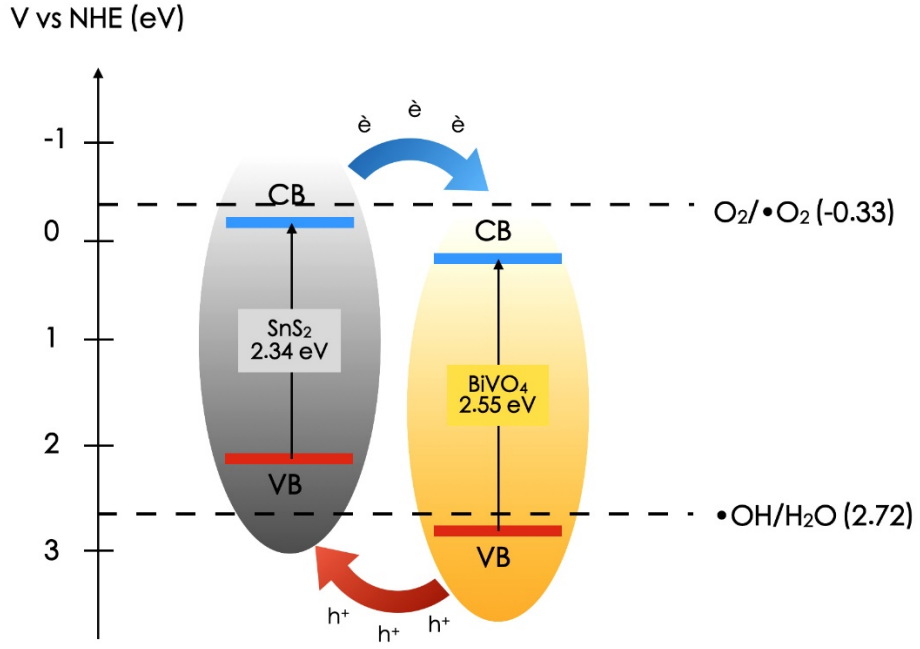

Figure 6 Schematic energy band diagram structure of SnS_2/$BiVO_4$ nanocomposite.

4. Conclusion

The effort of this article is made to synthesize $SnS_2/BiVO_4$ nanocomposite material via a facile sonochemical process with different SnS_2 loading content to enhance the photocatalytic performance of $BiVO_4$ under visible light illumination. The crystalline structures of all specimens exhibit the major $BiVO_4$ monoclinic phase and the SnS_2 hexagonal phase. It is found that different SnS_2 loading content exhibits significant influence on not only structural and morphological properties but also relevant optical properties of the $BiVO_4$ matrix in the form of a well-defined composite between two materials and increased specific surface area, leading to photocatalytic performance. The enhancement in photocatalytic performance is acknowledged by incorporating certain 0.05:1 ratio of SnS_2 loading content that could be due to the formation of heterojunction of the composite hindering the electron-hole pair recombination.

Acknowledgment

This work has been supported by the Thailand Research Fund (TRF) within the Royal Golden Jubilee Ph.D. Program (Grant no. PHD/0169/2561). We would like to thank College of Materials Innovation and Technology (CMIT), King Mongkut's Institute of Technology Ladkrabang for supported the facility.

References

[1] T. Saison, N. Chemin, C. Chanéac, O. Durupthy, L. Mariey, F. Maugé, V. Brezová, J. P. Jolivet, Insights into $BiVO_4$ properties as visible light photocatalyst, *J. Phys. Chem. C* **119** (2015) 12967-12977.

[2] G. Li, D. Zhang, J. C. Yu, Ordered mesoporous $BiVO_4$ through nanocasting: A superior visible light-driven photocatalyst, *Chem. Mater.* **20** (2008) 3983-3992.

[3] H. Li, K. Yu, X. Lei, B. Guo, H. Fu, Z. Zhu, Hydrothermal synthesis of novel $MoS_2/BiVO_4$ hetero-nanoflowers with enhanced photocatalytic activity and a mechanism investigation, *J. Phys. Chem. C* **119** (2015) 22681–22689.

[4] S. J. Hong, S. Lee, J. S. Jang, J. S. Lee, Heterojunction $BiVO_4/WO_3$ electrodes for enhanced photoactivity of water oxidation, *Energy Environ. Sci.* **4** (2011) 1781-1787.

[5] S. Kabouch, Y. Louafi, J. F. Bardeau, M. Trari, Synthesis, physical and semiconducting properties of SnS_2 prepared by chemical route, *J. Mater. Sci. Mater. Electron.* **30** (2019) 687-694.

[6] K. Dai, J. Lv. J. Zhang, C. Liang, G. Zhu, Band structure engineering design of g-C_3N_4/ZnS/SnS_2 ternary heterojunction visible-light photocatalyst with ZnS as electron transport buffer material, *J. Alloy. Compd.* **778** (2019) 215-223.

[7] W. Liu, L. Cao, G. Su, H. Liu, X. Wang, L. Zhang, Ultrasound assisted synthesis of monoclinic structured spindle $BiVO_4$ particles with hollow structure and its photocatalytic property, *Ultrason. Sonochem.* **17** (2010) 669-674.

[8] P. Intaphong, A. Phuruangrat, S. Thongtem, T. Thongtem, Sonochemical synthesis and characterization of BiOI nanoplates for using as visible-light-driven photocatalyst, *Mater. Lett.* **213** (2018) 88-91.

[9] C. Wattanawikkam, W. Pecharapa, Sonochemical synthesis, characterization, and photocatalytic activity of perovskite $ZnTiO_3$ nanopowders, *IEEE Trans. Ultrason. Ferroelect. Freq. Control* **63** (2016) 1663.

[10] T. Kansaard, K. N. Ishihara, W. Pecharapa, Characterization and visible light-driven photocatalytic activity of $BiVO_4$/BiOCl/Bi_2S_3 nanocomposites prepared by sonochemical process, *Phys. Status Solidi A* **220** (2023) 2200447.

[11] L. Zhou, W. Wang, L. Zhang, H. Xu, W. Zhu, Single-crystalline $BiVO_4$ microtubes with square cross-sections: Microstructure, growth mechanism, and photocatalytic property, *J. Phys. Chem. C* **111** (2007) 13659-13664.

[12] A. J. Khimani, S. H. Chaki, S. M. Chauhan, A. V. Mangrol, R. R. Meena, M. P. Deshpande, Synthesis, characterization, antimicrobial and antioxidant study of the facile sonochemically synthesized SnS_2 nanoparticles, *Nano-Struct. Nano-Objects* **18** (2019) 100286.

[13] H. Zhang, Y. Balaji, A. N. Mehta, M. Heyns, M. Caymax, I. Radu, W. Vandervorstb, A. Delabie, Formation mechanism of 2D SnS_2 and SnS by chemical vapor deposition using $SnCl_4$ and H_2S, *J. Mater. Chem. C* **6** (2018) 6172-6178.

[14] J. Xie, Y. Zhu, N. Zhuang, X. Li, X. Yuan, J. Li, G Hong, W. Mai, High-concentration ether-based electrolyte boosts the electrochemical performance of SnS_2–reduced graphene oxide for K-ion batteries, *J. Mater. Chem. A* **7** (2019) 19332-19341.

[15] T. D. Nguyen, Q. T. P. Bui, T. B. Le, T. M. Altahtamouni, K. B. Vu, D. N. Vo, N. T. H. Le, T. D. Luu, S. S. Hong, K. T. Lim, Co^{2+} substituted for Bi^{3+} in $BiVO_4$ and its enhanced photocatalytic activity under visible LED light irradiation, *RSC Adv.* **9** (2019) 23526-23534.

[16] J. Yu, A. Kudo, Effects of structural variation on the photocatalytic performance of hydrothermally synthesized $BiVO_4$, *Adv. Funct. Mater.* **16** (2006) 2163-2169.

[17] P. Ju, Y. Wang, Y. Sun, D. Zhang, Controllable one-pot synthesis of a nest-like $Bi_2WO_6/BiVO_4$ composite with enhanced photocatalytic antifouling performance under visible light irradiation, *Dalton Trans.* **45** (2016) 4588-4602.

[18] S. Xie, Q. Zhang, G. Liua, Y. Wang, Photocatalytic and photoelectrocatalytic reduction of CO_2 using heterogeneous catalysts with controlled nanostructures, *Chem. Commun.* **52** (2016) 35-59.

[19] A. Ebrahimi, N. Jafari, K. Ebrahimpour, M. Karimi, S. Rostamnia, A. Behnami, R. Ghanbari, A. Mohammadi, B. Rahimi, A Abdolahnejad, A novel ternary heterogeneous $TiO_2/BiVO_4$/NaY-Zeolite nanocomposite for photocatalytic degradation of microcystin-leucine arginine (MC-LR) under visible light, *Ecotox. Environ. Safe.* **210** (2021) 111862.

[20] H. She, H. Zhou, L. Li, Z. Zhao, M. Jiang, J. Huang, L. Wang, Q. Wang, Construction of a two-dimensional composite derived from TiO_2 and SnS_2 for enhanced photocatalytic reduction of CO_2 into CH_4, *ACS Sustainable Chem. Eng.* **7** (2019) 650-659.

[21] K. Pingmuang, J. Chen, W. Kangwansupamonkon, G. G. Wallace, S. Phanichphant, A. Nattestad, Composite photocatalysts containing $BiVO_4$ for degradation of cationic dyes, *Sci. Rep.* **7** (2017) 8929.

[22] X. Cao, Y. Gu, H. Tian, Y. Fang, D. Johnson, Z. Ren, C. Chen, Y. Huang, Microemulsion synthesis of *ms/tz*-$BiVO_4$ composites: The effect of pH on crystal structure and photocatalytic performance, *Ceram. Int.* **46** (2020) 20788-20797.

[23] H. Xu, Y. Wang, X. Dong, N. Zheng, H. Ma, X. Zhang, Fabrication of In_2O_3/In_2S_3 microsphere heterostructures for efficient and stable photocatalytic nitrogen fixation, *Appl. Catal. B Environ.* **257** (2019) 117932.

[24] S. Meng, T. Ogawa, H. Okumura, K. N. Ishihara, Enhanced photocatalytic activity of $BiVO_4/Bi_2S_3/SnS_2$ heterojunction under visible light, *Catalysts* **10** (2020) 1294.

[25] H. L. Tan, R. Amal, Y. H. Ng, Alternative strategies in improving the photocatalytic and photoelectrochemical activities of visible light-driven $BiVO_4$: A review, *J. Mater. Chem. A* **5** (2017) 16498-16521.